

THE EXTENDED NARROW-LINE REGION OF THE SEYFERT 1 GALAXY ESO 362-G18 VERSUS THAT OF THE SEYFERT 2 GALAXY ESO 362-G8

HENRIQUE A. FRAQUELLI AND THAISA STORCHI-BERGMANN
Instituto de Física, UFRGS, 910501-970 Porto Alegre, RS, Brazil

AND

LUC BINETTE
Instituto de Astronomía, UNAM, Ap. 70-264, 04510 DF, Mexico
Received 1999 August 26; accepted 1999 November 10

ABSTRACT

We use long-slit spectroscopic data to study in detail the extended narrow-line regions (ENLRs) of the Seyfert 1 galaxy ESO 362-G18 and Seyfert 2 galaxy ESO 362-G8. These two galaxies have similar emission-line luminosities and extents of the ENLR (~ 4 kpc), whose shapes in previous narrowband [O III] images suggest anisotropic escape of the nuclear ionizing radiation as expected for shadowing by a nuclear torus in the framework of the unified model. In the Seyfert 1 galaxy the high-excitation gas shows an approximately cone-shaped morphology. From the observed kinematics, we conclude that the gas within the cone most probably belongs to the galaxy disk, which implies that the collimation axis is closer to the disk than half the opening angle of the cone of ionizing radiation. In the Seyfert 2 galaxy, the main structure in the high-excitation gas is an emission blob which apparently consists of a high-latitude cloud being blown away from the nuclear region and ionized by the nuclear source.

We use the radial distribution of stellar population features in order to extrapolate this population to the nucleus and isolate the optical continuum of the nuclear source. We obtain a featureless power-law continuum $F_\nu \propto \nu^{-0.76}$ for the Seyfert 1 galaxy, while for the Seyfert 2 galaxy we conclude that the nuclear bluer color and smaller equivalent widths of the absorption lines are due to an aging burst of star formation (age ≈ 300 Myr) and that the nuclear source is hidden from direct view.

Using the photoionization code MAPPINGS Ic and a mixture of matter-bounded (MB) and ionization-bounded (IB) clouds, we model the ENLRs of the two galaxies. We use all the observables, mostly the emission-line fluxes as a function of distance from the nucleus and the optical nuclear continuum observed in the Seyfert 1 galaxy as well as its X-ray flux, to constrain the parameters of a self-consistent model for the ENLR. For both galaxies, we conclude that a power-law ionizing continuum $F_\nu \propto \nu^{-1.2}$ better reproduces the high-excitation lines near the nucleus than a multisegmented power law used in previous works. For the Seyfert 1 galaxy ESO 362-G18, the inferred luminosity of the ionizing continuum can be reconciled with the flux observed in the optical, while in the X-rays the observed flux is ~ 100 times weaker than that necessary to reproduce the line fluxes, suggesting that the X-ray continuum is absorbed toward Earth. For the Seyfert 2 galaxy ESO 362-G8, the inferred ionizing continuum when extrapolated to the optical implies a minimum obscuration toward the nuclear source of $A_V \approx 4.0$ mag.

In the hypothesis of an isotropic nuclear source, in order to better constrain the model parameters, we have adopted symmetrical physical conditions as a function of distance on both sides of the nucleus: namely, the ionizing flux, the temperature, density, and ionization parameter of the MB gas, and the metallicity. The radial density behavior of the IB gas was observationally inferred from the [S II] doublet ratio. The only free parameter, which was allowed to vary independently, was the relative proportion of the MB and IB emission-line components along the ENLR. The high-excitation gas within the cone of ESO 362-G18 and within the blob of ESO 362-G8 have been modeled as regions of larger mass contribution from the MB component relative to other locations of the ENLR.

We derive the filling factors, covering factors, and gas masses along the ENLR as a function of distance from the nucleus. A comparison between the model results for the two galaxies shows that, around the nucleus, the Seyfert 1 galaxy has a larger excitation due to a larger contribution of the MB component. However, in the cone, the excitation is lower than in the blob of the Seyfert 2 galaxy due to a combination of a lower ionizing flux and larger gas density in the disk of the Seyfert 1 galaxy. The total ionized gas mass derived for the blob in the Seyfert 2 galaxy is $10^{5.8} M_\odot$, consistent with its proposed origin in a nuclear superwind which probably occurred ~ 300 Myr ago, while the ionized gas mass in the disk of the Seyfert 1 galaxy is 1 order of magnitude smaller.

Subject headings: galaxies: active — galaxies: ISM — galaxies: nuclei — galaxies: Seyfert

1. INTRODUCTION

Many works have been dedicated in the past to the modeling and interpretation of the narrow-line region (NLR) in active galactic nuclei (AGNs) (Ferland & Netzer 1983;

Binette, Wilson, & Storchi-Bergmann 1996; Binette et al. 1997; Storchi-Bergmann et al. 1998; Rodríguez-Ardila, Pastoriza, & Maza 1998; Alexander et al. 1999). Photoionization is believed to be the dominant excitation mechanism in

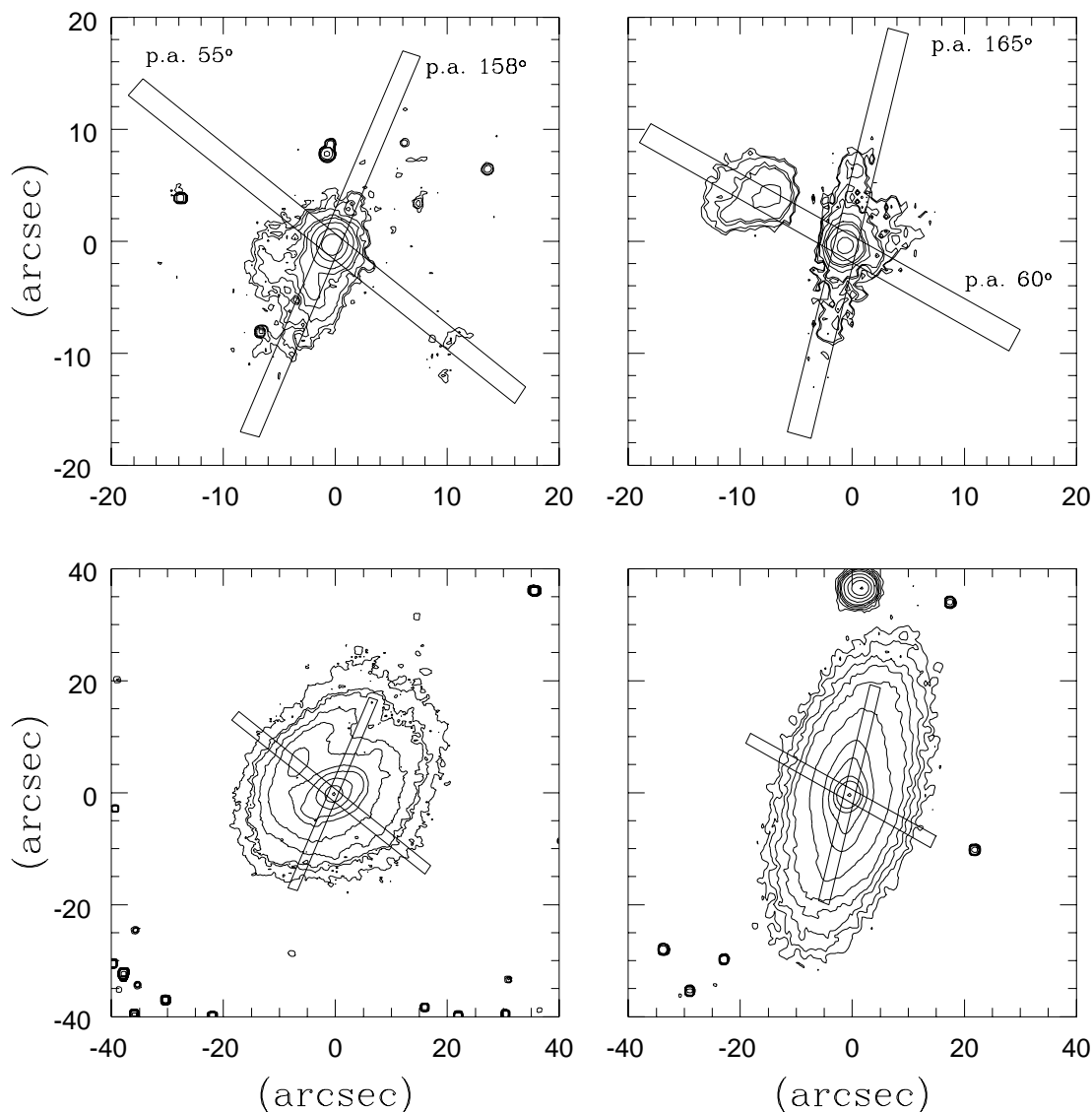


FIG. 1.—Contour plots of [O III] (*top*) and green continuum (*bottom*) images for ESO 362-G18 (*left*) and ESO 362-G8 (*right*) together with a representation of the long slits used in this work. (Courtesy of Mulchaey et al. 1996.)

NLRs of AGNs, although other mechanisms may also play a role (as reviewed in Viegas & de Gouveia Dal Pino 1992). Photoionization models can also be applied to the extended narrow-line region (ENLR) (Unger et al. 1987), where it is possible to resolve spatially the emitting region (e.g., Nazarova, O’Brien, & Ward 1997; Nazarova et al. 1998). In the ENLR, unlike the NLR, it is possible to constrain parameters such as cloud geometries and densities, reducing the number of free parameters in the models.

Models with a single density n and a single ionization parameter U (defined as the ratio of the ionizing photons density to the gas density) of the NLR, although broadly successful in fitting strong optical lines, are unsatisfactory in important aspects such as predicting too weak high-excitation lines, too low electronic temperatures, and too small a range in $\text{He II}/\text{H}\beta$. Interestingly enough, the same inadequacies of models (as for the NLR) are found for the extended gas of the ENLR.

To overcome the above problems, Binette et al. (1996) proposed that the ENLR could contain a combination of

matter-bounded (MB) and ionization-bounded (IB) clouds. These two cloud populations have different spectra which can be combined to reproduce a wide range of observed ENLR spectra. The main innovation was to assume that the IB clouds are photoionized by radiation from the central source which has been filtered and attenuated by the intervening MB component. This ensures that the IB component is of lower excitation (no He II , for instance, but significant [O I] and [S II] lines).

In this paper, we use the code MAPPINGS Ic (Binette et al. 1997) to model the high-excitation gas in the ENLR of two Seyfert galaxies, ESO 362-G18 and ESO 362-G8. The two galaxies have similar emission-line luminosities and extents of the ENLR, but ESO 362-G18 is a Seyfert 1 galaxy (with $M_B = -19.73$) in which both the nuclear continuum and the broad-line region (BLR) can be observed. It is located at 50.4 Mpc ($H_0 = 75 \text{ km s}^{-1} \text{ Mpc}^{-1}$) such that $1''$ corresponds to 233 pc at the galaxy. ESO 362-G8 is a Seyfert 2 galaxy (with $M_B = -20.42$) in which the nuclear source appears hidden (on account of the observed contin-

TABLE 1
LOG OF OBSERVATIONS

Galaxy	Date	P.A. (deg)	Air Mass	Exposure Time (s)	Window Center (arcsec)	Window Area (arcsec ²)	
ESO 362-G18	1994 Dec 8	158	1.02	600	Nucleus, NW2, SE2	2 × 2	
				1800	NW5, SE5	4 × 2	
	1994 Jan 7	55	1.25	600	NW10, SE10	6 × 2	
				600	NW17, SE17	8 × 2	
ESO 362-G8	1994 Dec 8	60	1.02	600	NE2, SW2, SW4	2 × 2	
				600	NE5, SW7, SW11	4 × 2	
	1994 Jan 7	165	1.17	600	NE10	6 × 2	
				600	Nucleus, 2 SW, 2 NE	2 × 2	
				600	SW4, NE4, NE6	4 × 2	
				600	NE9	6 × 2	
					600	NE14	8 × 2
					600	SE2, SE4, NW2	2 × 2
				600	NW5, SE7	4 × 2	
				600	NW10, NW16, SE12	6 × 2	
				600	SE19	8 × 2	

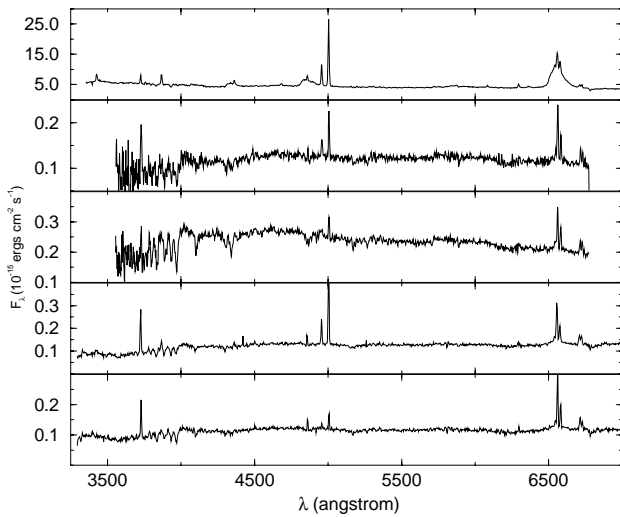


FIG. 2.—Extracted spectra of ESO 362-G18. From top to bottom: Nucleus, NE10'', SW7'', SE10'' (“cone”), and NW10''.

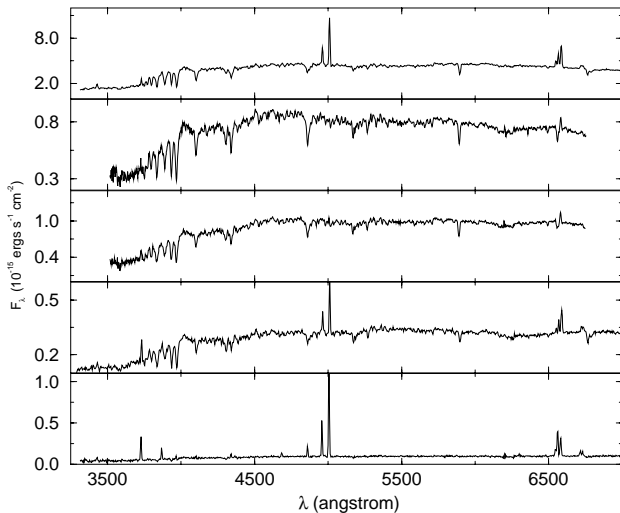


FIG. 3.—Extracted spectra of ESO 362-G8. From top to bottom: Nucleus, SE7'', NW5'', SW4'', and NE9'' (“blob”).

uum energy distribution; see § 3), in accordance with the unified model scenario (Antonucci 1993). The galaxy is located at 64.4 Mpc with 1'' corresponding to 298 pc.

Broadband and narrowband images in [O III] λ 5007, H α + [N II] λ 6548, 6584 and excitation maps for both galaxies have been obtained by Mulchaey, Wilson, & Tsvetanov (1996). Contour plots of the [O III] and green continuum images obtained by these authors are reproduced in Figure 1. For ESO 362-G18, the [O III] image is asymmetric with a cone-shaped structure extending to \sim SE10'' from the nucleus. The H α + [N II] image shows a more symmetric emission distribution and a similar extent. In the excitation map, the highest excitation is observed at the nucleus and in the cone at \sim SE7'' from the nucleus. For ESO 362-G8, the [O III] image is extended mostly along the major axis of the galaxy at position angle (P.A.) 165° and along the perpendicular direction. The most conspicuous structure is a blob of intense emission at \sim ENE10''. The blob is also present in the H α + [N II] image which is, however, more symmetric and extends up to \sim 20'' from the nucleus.

We have used optical long-slit spectra of the above two galaxies in order to model the line fluxes of the ENLR, using the two-component model described above, allowing for the attenuation and dilution of the central ionizing continuum as a function of distance from the nuclei. In order to isolate the nuclear continuum, the stellar population contribution has been evaluated by comparing the nuclear and extranuclear stellar absorption features. After correcting the spectra for the contribution of the stellar population, we model the gas emission in a self-consistent way, using all the observational constraints available. These include the emission-line fluxes and ratios for both galaxies as a function of distance from the nucleus as well as the observed nuclear continuum for the Seyfert 1 galaxy. We derive the filling and covering factors, the gas densities and masses of the emitting gas, and the luminosity of the ionizing source.

In § 2 we describe the observations and the reduction techniques, in § 3 we characterize the stellar population and isolate the nuclear continuum, in § 4 we derive the gas and stellar kinematics, in § 5 we characterize the emission-line

properties and distributions, which are modeled in § 6, and in § 7 we present the conclusions.

2. OBSERVATIONS

High signal-to-noise ratio long-slit spectra of the two galaxies were obtained using the 4 m telescope, Cassegrain Spectrograph, and a Reticon CCD detector at the Cerro Tololo Inter-American Observatory (CTIO) on the nights of 1994 January 7 and December 8. The seeing was $\sim 1''$, the spectral resolution $\sim 4 \text{ \AA}$, and the spectral range of the observations was 3300–7450 \AA . The slit width corresponded to $2''$ in the sky, and the scale of the frames in the spatial direction was $1'' \text{ pixel}^{-1}$. The slit was oriented to include both the nucleus and blob in ESO 362-G8 and the nucleus and the apparent cone in ESO 362-G18. Two additional long-slit spectra were also obtained approximately along the perpendicular direction to the previous ones. Figure 1 illustrates the slit orientations relative to the high-excitation gas and green continuum. In order to minimize effects of differential atmospheric refraction (Filippenko 1982), the observations were scheduled so that the slit orientation was always close to the parallactic angle.

The spectra were reduced using standard procedures in IRAF. There is some second-order contamination for wavelengths larger than 6000 \AA , but the effect is only noticeable in the continuum and does not affect the emission lines. One-dimensional spectra were extracted binning together, from 2 pixels (in the inner regions) to 8 pixels (in the outer regions). A log of observations is shown in Table 1, which gives the date of observation, slit P.A., air mass, exposure time, location, and dimension of the extraction window. Hereafter, whenever we refer to a window, we will use its center as the corresponding location. Figures 2 and 3 show samples of extracted spectra.

3. STELLAR POPULATION AND NUCLEAR CONTINUUM

Both galaxies present stellar absorption features. In ESO 362-G8 these features are prominent both at the nucleus and outside the nucleus, while in ESO 362-G18 they are more prominent outside the nucleus.

The main stellar features identified in the spectra were the absorptions of Ca II K, G band, and Mg I as well as high-order Balmer absorption lines. Following the methodology of previous works (e.g., Cid Fernandes, Storch-Bergmann, & Schmitt 1998), we have measured the equivalent widths (W_λ) of the first three lines as well as the ratio between the continuum fluxes at 5870 and 4020 \AA as a function of distance to the nucleus (Figs. 4 and 5).

The run of the W_λ of the absorption lines with distance shows a decrease toward the nucleus in both cases. This decrease is usually interpreted as due to a blue continuum present in the nucleus which dilutes the absorption lines. This behavior has been observed in several other Seyfert galaxies and can be due to either a featureless Seyfert 1 continuum or a contribution from a young stellar population (Cid Fernandes et al. 1998).

We have constructed stellar population templates for the nuclear spectra with the goal of isolating the nuclear continuum. For ESO 362-G8, the template was obtained averaging the extranuclear spectra at NW10'', NW16'', and SE12'', while for ESO 362-G18, we have averaged the spectra at NE10'' and SW11''. In the cases in which there were residual emission lines in the templates, these were eliminated using

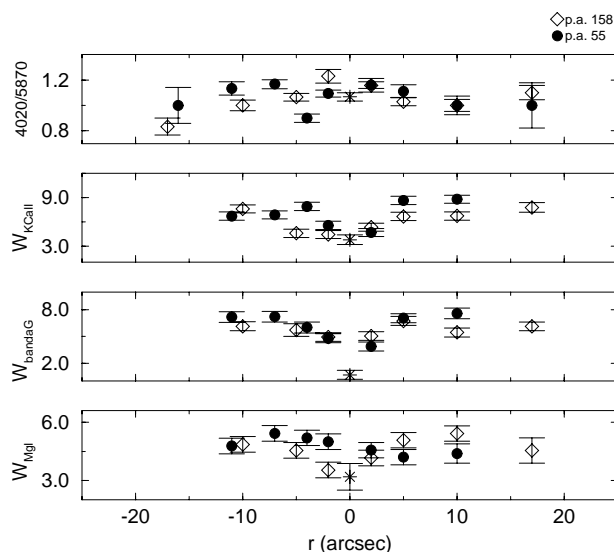


FIG. 4.—Equivalent widths and continuum ratio $\lambda 4020/\lambda 5870$ as a function of distance from the nucleus for ESO 362-G18. The locations at P.A. 158° are represented as open diamonds while those at P.A. 55° are represented as filled circles. The nucleus is identified as a star. Negative r is to the southeast and northeast, and positive r is to the northwest and southwest.

emission-free spectra from the library of Bica (1988) as reference to interpolate the templates in the edited regions (Storch-Bergmann et al. 1996b). This procedure is preferable to the direct use of Bica's templates because of their lower spectral resolution ($\sim 15 \text{ \AA}$) than in our observations.

The templates were then redshifted to the radial velocities of the nuclei of both galaxies, normalized at 5152 \AA , and subtracted from the nuclear spectra (Figs. 6 and 7). The normalization factor used to multiply the stellar population template before the subtraction was the ratio between the nuclear and template values of $W_{\text{Mg I}}$. The resulting stellar population fraction at 5152 \AA was $\approx 50\%$ for ESO 362-G18.

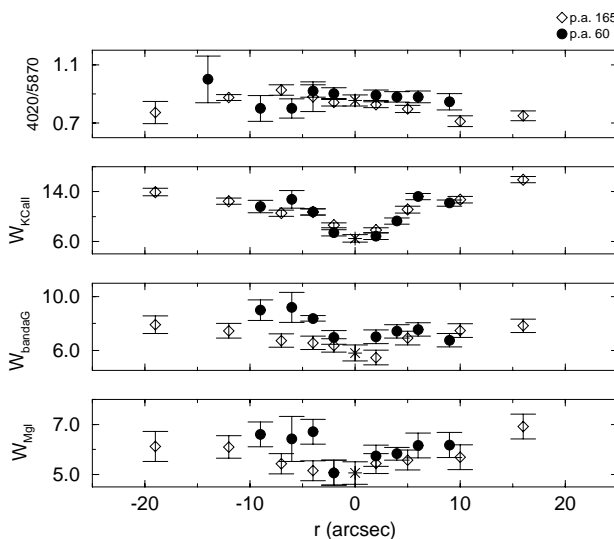


FIG. 5.—Equivalent widths and continuum ratio $\lambda 4020/\lambda 5870$ as a function of distance from the nucleus for ESO 362-G8. The locations at P.A. 165° are represented by open diamonds while those at P.A. 60° are represented by filled circles. The nucleus is identified as a star. Negative r is to the southeast and northeast, and positive r is to the southwest and northwest.

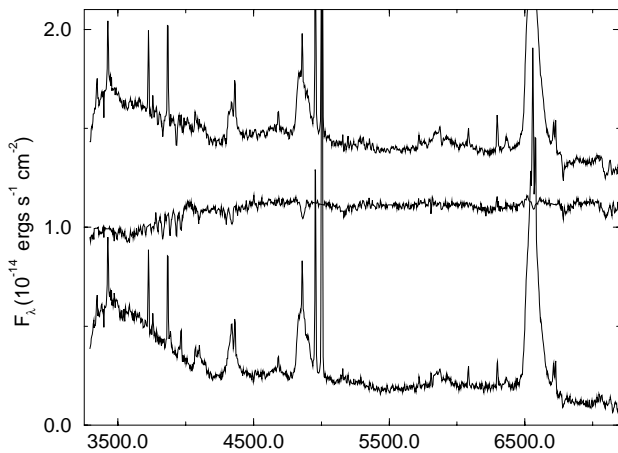


FIG. 6.—*Top*: Nuclear spectrum of ESO 362-G18. *Middle*: Stellar population template normalized to 50% of the nuclear continuum at 5152 Å. *Bottom*: The difference between the two. The top and the middle spectra have been shifted vertically for a better visualization of the difference spectrum, which is plotted in the rest frame of the galaxy.

For ESO 362-G8, the resulting stellar population fraction at 5152 Å was $\approx 80\%$. The template presented a bluer continuum than the nucleus, which we interpreted as due to reddening of the nuclear spectrum. This interpretation is reinforced by the much larger $W_{\text{Na I}}(\lambda 5893)$ in the nucleus as compared to the template value, while the values of W of the other metallic absorptions are smaller than those of the template. It is well known that the Na I line is a reddening indicator because it is produced not only in stellar atmospheres but also in the interstellar medium (Bica & Alloin 1986b; see also Storchi-Bergmann, Mulchaey, & Wilson 1992a). We have then dereddened the nuclear spectrum by the minimum $E(B-V)$ which was required to bring the nuclear continuum higher at all wavelengths than the template after normalization of the two spectra in the red. Such normalization can be justified by the fact that the slopes beyond $\lambda \approx 5340$ Å do not change significantly for different stellar populations (Bica & Alloin 1986b). The deduced reddening was $E(B-V) = 0.25$. The template was then sub-

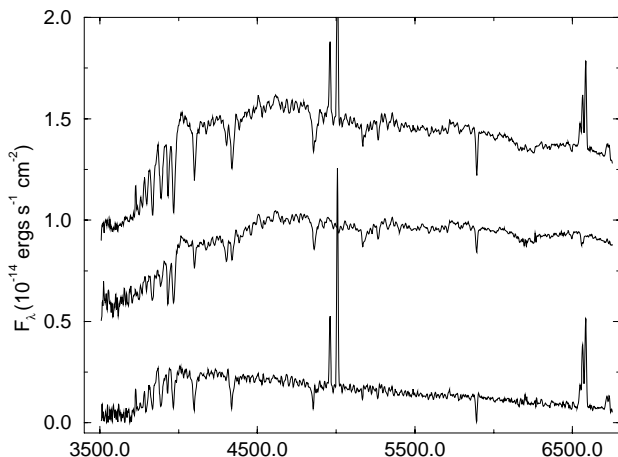


FIG. 7.—*Top*: Dereddened nuclear spectrum of ESO 362-G8. *Middle*: Stellar population template normalized to 80% of the nuclear continuum at 5152 Å. *Bottom*: The difference between the two. The top and the middle spectra have been shifted vertically for a better visualization of the difference spectrum, which is plotted in the rest frame of the galaxy.

tracted from the nuclear spectrum after its normalization to 80% of the nuclear flux at 5152 Å.

For ESO 362-G18, the residual nuclear minus template spectra is a featureless continuum, while for ESO 362-G8, deep residual Balmer absorption lines and continuum ratios characteristic of a stellar population with ages between 100 and 500 Myr (Bica & Alloin 1986a) are found. It can thus be concluded that while in ESO 362-G18 the dilution of the W_λ is due to the AGN continuum, in ESO 362-G8, the dilution is due to an intermediate-age burst of star formation in the nucleus. From the run of $W(\text{K Ca II})$ in Figure 5, it can be concluded that the burst actually extends up to 5" (~ 1.5 kpc) from the nucleus.

Other cases of dilution observed in Seyfert 2 galaxies by Cid Fernandes et al. (1998) were also concluded to be due to young to intermediate-age stellar components (Storchi-Bergmann et al. 1998). In fact, Schmitt et al. (1997), using spectral synthesis, found that such an intermediate-age component seems to be a common characteristic of Seyfert 2 nuclear spectra. An important signature of a 100–500 Myr stellar population is the presence of high-order Balmer absorption lines (see also González Delgado, Leitherer, & Heckman 1999). In Figures 2 and 3 it can be observed that such signature is present not only in the nuclear and extranuclear spectrum of the Seyfert 2 galaxy but also in the extranuclear spectrum of the Seyfert 1 galaxy.

We do not find any evidence for a featureless continuum in the Seyfert 2 galaxy contributing more than 5% in the near-UV, implying that the nuclear source is thus hidden from direct view (in agreement with the unified model).

The featureless continuum of ESO 362-G18 was well fitted by a power law $F_\nu \propto \nu^{-0.76}$ between 4200 and 6200 Å. For $\lambda \leq 4200$ Å, there are additional components which can be due to the Balmer continuum, [Fe II] emission, and a possible weak blue bump.

4. KINEMATICS

To map the gas kinematics, we have averaged together the central wavelengths of Gaussians which we fitted to the emission lines [O II] $\lambda 3727.5$, [O III] $\lambda 5006.8$, and [N II] $\lambda 6583.6$. In order to map also the stellar velocities, we used the central wavelengths of the absorption features which could be well fitted by Gaussians: Ca II K $\lambda 3933.7$, Na I $\lambda 5893.0$, and in a few cases, H δ . With an average spectral resolution (adopted as the FWHM of the sky emission lines) of ≈ 250 km s $^{-1}$, we estimate the maximum uncertainty in our measurements to be $\approx \pm 50$ km s $^{-1}$. The resulting velocities along the two position angles of our spectra are shown in Figures 8 and 9.

For ESO 362-G18 (Fig. 8), it is observed that the gas and stellar kinematics are in approximate agreement. Along P.A. 158° the velocities are consistent with circular rotation observed at an orientation not far from the major axis. Indeed, in the ESO catalog the P.A. of the photometric major axis is 160°, while Mulchaey et al. (1996) derive P.A. = 149° from their green continuum image (Fig. 1).

Using the ratio between the minor and major photometric axis from Winkler (1997), we derive an approximate inclination of 37° for ESO 362-G18, which leads to a total velocity amplitude of ≥ 330 km s $^{-1}$. The southeast side—where the emission cone is located—is approaching while the opposite side is receding. The gas inside the cone shares the same kinematics as the rest of the galaxy, which suggests that it is located in the plane of the galaxy. A possible

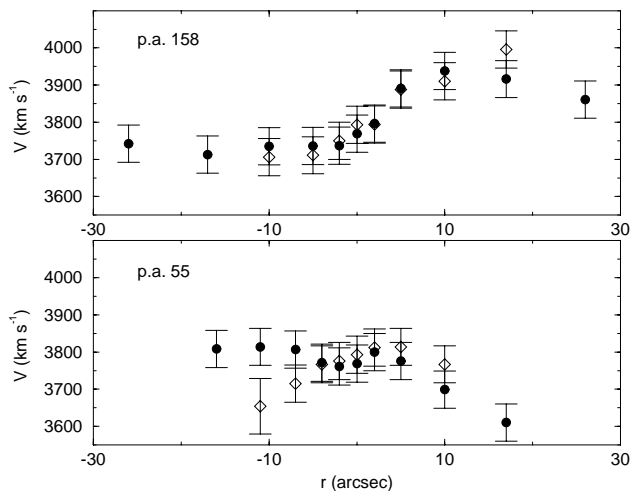


FIG. 8.—Heliocentric velocities of ESO 362-G18. The gaseous component is represented by filled circles while the stellar component is represented by open diamonds. Negative r is to the southeast and northeast, and positive r is to the northwest and southwest.

geometry could be that the AGN collimating axis is oriented at an angle with respect to the galactic plane which allows the nuclear radiation to intercept the gas in the disk but, at the same time, also allows the visualization of the nuclear continuum and BLR. This could happen, for example, if the opening angle of the ionizing radiation cone is larger than 60° and the collimating axis makes an angle with the galaxy plane $\leq 30^\circ$. The geometry would be similar to that proposed for NGC 4151 (Robinson et al. 1994), for example, in which the cone of ionizing radiation intercepts the disk but both the nuclear continuum and the BLR can be observed.

Along P.A. 55° , the velocity behavior at the central region is similar to that expected for an orientation close to the minor axis of the galaxy except for two deviant points: the stellar velocity at NW11" and the gas velocity at SW17". The latter corresponds to an isolated faint knot of relatively strong [O III] emission, as shown in Figure 1. In this same

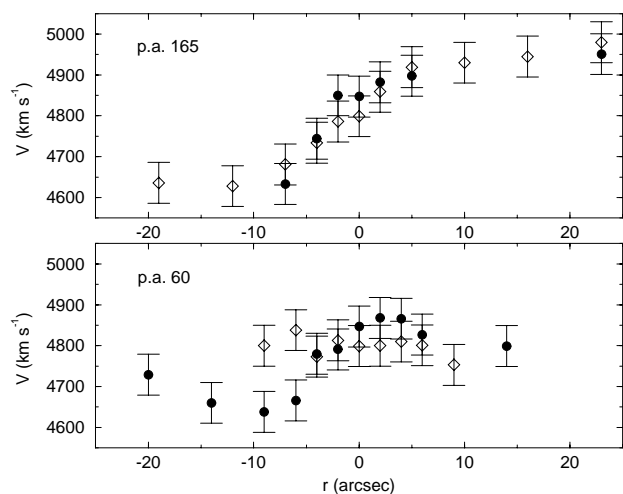


FIG. 9.—Heliocentric velocities of ESO 362-G8. The gaseous component is represented by filled circles while the stellar component is represented by open diamonds. Negative r is to the southeast and northeast, and positive r is to the northwest and southwest.

figure, it can be observed that the deviant stellar velocity corresponds to the location of what appears to be a tidal arm apparently originated from the interaction of ESO 362-G18 with ESO 362-G17, a galaxy located SW373" (Soares et al. 1995).

For ESO 362-G8 (Fig. 9), along P.A. 165° the gas and the stars also present a rotation curve consistent with circular motion in the plane of the galaxy. The southeast side is approaching while the northwest is receding. The above P.A. is the same as that of the photometric major axis (Mulchaey et al. 1996 and Fig. 1). For an inclination of 62° (Braatz, Wilson, & Henkel 1997), the resulting deprojected total velocity amplitude is $\approx 360 \text{ km s}^{-1}$. Along P.A. 60° , the stellar kinematics—showing almost no velocity variation—is consistent with that expected for an orientation close to the minor axis. On the other hand, the gas in the blob (NE6"–NE14") is blueshifted by up to 150 km s^{-1} relative to the stellar velocities. This suggests that the blob is not located in the galactic plane. The low reddening presented by the gas in the blob (§ 5) favors a location between the disk of the galaxy and Earth. The gap between the nucleus and the blob in the [O III] image (Fig. 1) and the presence of the blob also in the H α image distorting the shape of the outermost contours, as observed by Mulchaey et al. (1996), supports this interpretation. This geometry could be expected if the blob corresponds to a cloud at high galactic latitudes blown away from the inner regions of the galaxy and projected against the far side of the galaxy. In this case, the collimating axis would be oriented close to the minor axis of the galaxy. This geometry is apparently similar to that producing the ionization cone observed, for example, in NGC 3281 (Storchi-Bergmann, Wilson, & Baldwin 1992b).

5. EXCITATION AND REDDENING OF THE EMISSION-LINE GAS

We now discuss the gas emission properties of the two galaxies along the directions at which the high-excitation gas is most extended: along the "cone" in ESO 362-G18 (P.A. 158°) and along the direction of the "blob" in ESO 362-G8 (P.A. 60°).

For ESO 362-G18, the extinction of the ENLR was deduced from the observed H α /H β intensity ratio assuming an intrinsic H α /H β = 3.1 (Osterbrock 1989).

For ESO 362-G8, H β is too weak to be measured (frequently not filling the absorption feature), except at the blob. But the strength of H α indicates that the ratio H α /H β is certainly larger than 3.1 in the inner region. In addition, we have concluded in § 3 that the nuclear stellar population is reddened by $E(B-V) \sim 0.25$. As an alternative to the H α /H β ratio we have decided to use the line ratio [N II] $\lambda 6548$, 6563/[O II] $\lambda 3727$ to calculate the reddening. In order to do this, we assumed that the N/O abundance ratio is constant along the ENLR, and thus [N II]/[O II] should not vary along the ENLR, as both ions have similar ionization and excitation potentials. The adopted "intrinsic" value for the [N II]/[O II] line ratio was that corresponding to the outermost location within the blob, which presents very little reddening, as inferred from the H α /H β ratio (which can only be measured at the blob). The adopted intrinsic [N II]/[O II] ratio had to be corrected for this residual reddening.

The resulting reddening values as a function of distance from the nucleus are shown in Figures 10 and 11. For ESO

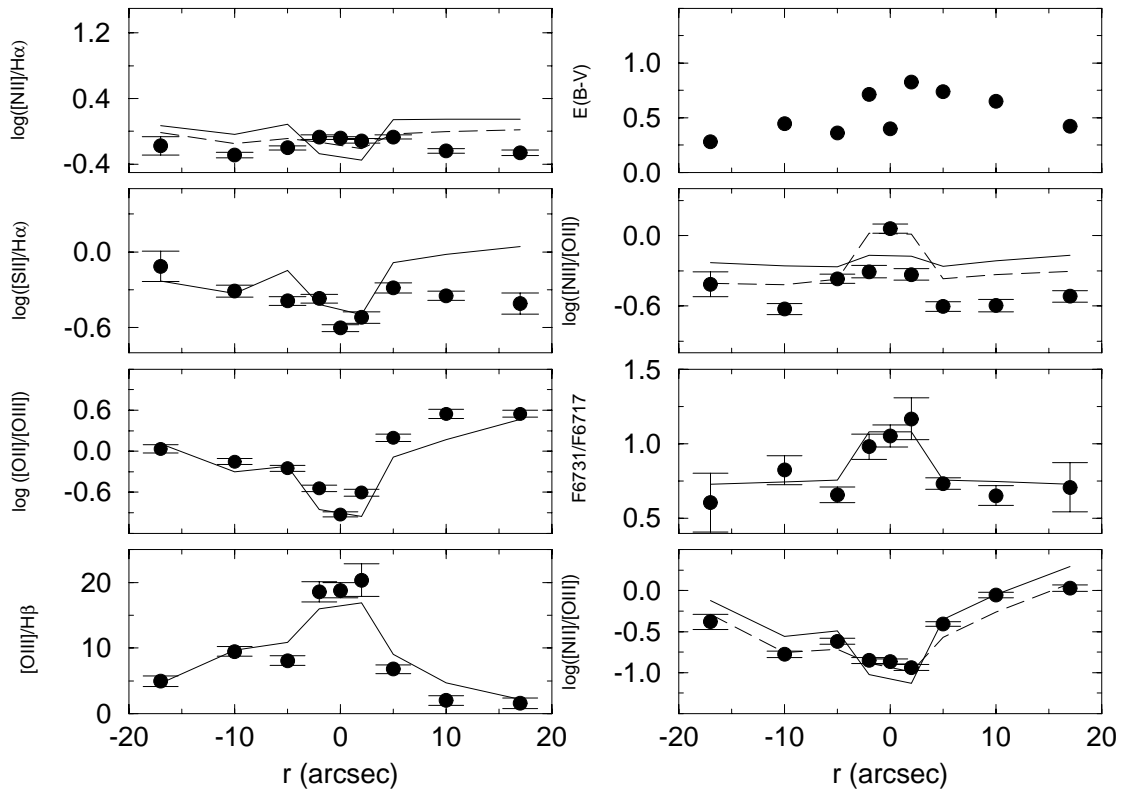


FIG. 10.—Observed (*circles*) and modeled (*lines*) emission-line ratios for ESO 362-G18 (P.A. 158°) and $E(B-V)$ values as a function of the distance from the nucleus. Dashed lines correspond to the modified elements abundances described in the text. Negative r is to the southeast (cone), and positive r is to the northwest.

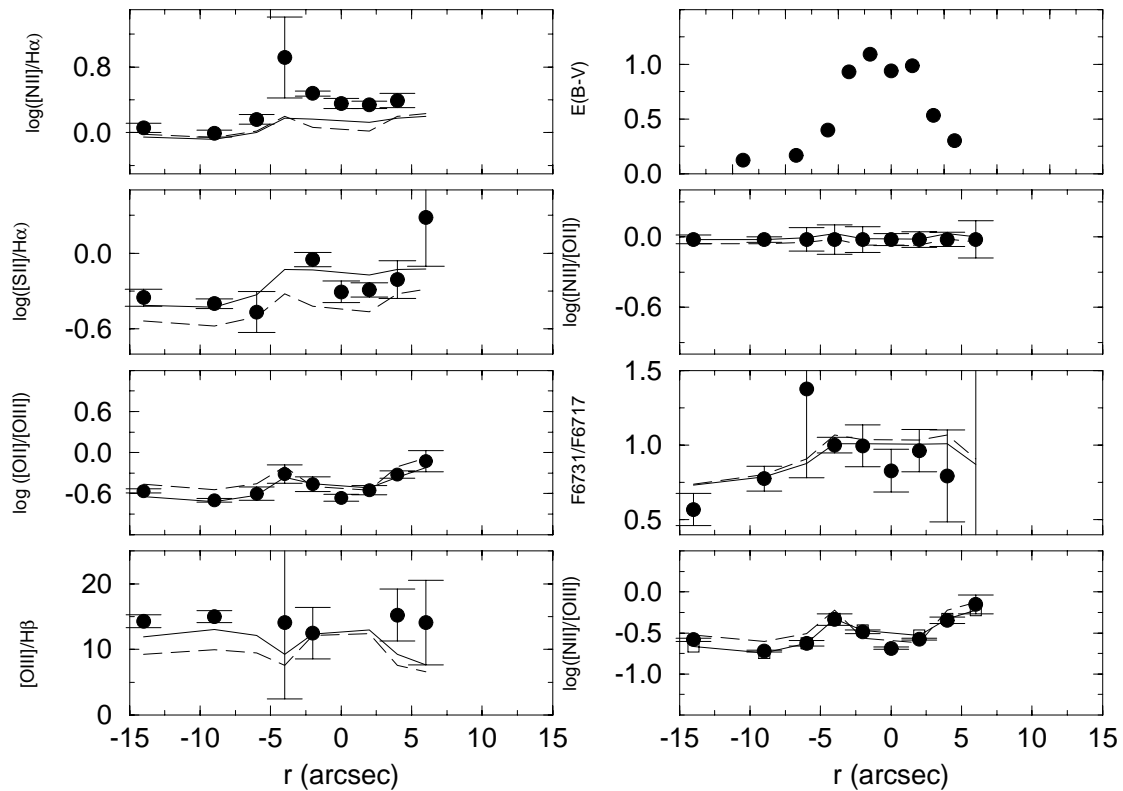


FIG. 11.—Observed (*filled circles*) and modeled (*lines*) emission-line ratios for ESO 362-G8 (P.A. 60°) and $E(B-V)$ values as a function of distance from the nucleus. The solid lines correspond to the power-law ionizing continuum, while the dashed lines correspond to the MFK continuum. Negative r is to the northeast (blob), and positive r is to the southwest.

362-G18, the nucleus and the cone region present the lowest reddenings [$E(B-V) \approx 0.4$], while other locations reach $E(B-V) \approx 0.8$. For ESO 362-G8, the reddening is large [up to $E(B-V) = 1$] within $5''$ from the nucleus decreasing outward down to ≈ 0 inside the blob.

The spectra of the nucleus and ENLR of the two galaxies show both high-excitation lines, such as [O III] $\lambda\lambda 4959, 5007$ up to [Ne V] $\lambda 3426$, and low-excitation lines, such as [O II] $\lambda\lambda 3727, 4454$, [N II] $\lambda\lambda 6548, 6583$, and [S II] $\lambda\lambda 6717, 6731$. [Ne V] $\lambda 3426$ and [O III] $\lambda 4363$ are detected at the nucleus and at $2''$ from it in ESO 362-G18 while in ESO 362-G8 we only detect [O III] $\lambda 4363$ at the blob.

Figure 10 shows the variation of emission-line ratios as a function of distance from the nucleus for ESO 362-G18. The ratio [O II]/[O III] presents a minimum at the nucleus, increasing farther out; [O III]/H β peaks at the nucleus (~ 19), decreasing outward. To the southeast, the [O III]/H β values are higher and those of [O II]/[O III] and [N II]/[O III] are lower than to the northwest, consistent with the presence of the ionization cone to southeast. The [Ne V]/H β , He II/H β , and [O III] $\lambda 4363$ /[O III] $\lambda 5007$ ratios can be measured only in the nuclear spectrum and at $2''$, with values ≈ 2.00 , ≈ 0.70 , and ≈ 0.02 .

Figure 11 shows the variation of emission-line ratios as a function of distance from the nucleus for ESO 362-G8. Due to the weakness of H β emission and the strong underlying absorption, the H β flux was calculated from the reddening-corrected H α flux, using a flux ratio $F_{H\alpha}/F_{H\beta} = 3.1$. All the emission-line ratios show an approximately symmetric behavior on both sides of the nucleus up to $\approx 5''$: [O II]/[O III] and [N II]/[O III] show a minimum at the nucleus, while [N II]/H α and [S II]/H α show a similar trend; [O III]/H β seems not to vary much, although the errors are large due to the weakness of H β . Toward the blob the line ratios present a discontinuity: [N II]/H α , [S II]/H α , [O II]/[O III], and [N II]/[O III] decrease, indicating a higher excitation, also revealed by the high [O III]/H β and consistent with the [O III] image (Fig. 1).

6. MODELING

We modeled the extended gaseous emission using the code MAPPINGS Ic, assuming that the ENLR consists of a mixture of MB and IB components (Binette et al. 1996). This model has two (*not* mutually exclusive) geometrical representations: in one case (1) we have a system of somewhat higher density gas condensations (the IB component) embedded in a low-density gas envelope (the MB component); in the other (2) the IB component consists of independent clouds which lie at somewhat greater distance behind the intervening MB clouds. In both cases, the IB component sees radiation “filtered” by the MB component and its ionization parameter is further reduced by being either (1) of higher density or (2) exposed to a more diluted radiation.

We emphasize that individually either component of the IB/MB tandem is very small physically and occupies a relatively small volume of the ionizing cone, and therefore both components can be present at any radii along the cone. Because of this small size, the assumed plane-parallel geometry in the photoionization calculations of the emission-line spectrum of either component is entirely justified. A grid of such MB and IB components was calculated. For a given extraction window, the appropriate IB and MB components were selected (see constraints below), summed,

and then scaled to match the observed line luminosity and ratios.

Two different ionizing continuum distributions were explored: a multisegmented power law as in Matthews & Ferland (1987) with a spectral index less steep ($\alpha = -2$) in the region between 56.2 and 365 eV (Korista, Ferland, & Baldwin 1997, hereafter MFK continuum) and a single-index power law of the form $F_\nu = kv^{-\alpha}$, as in Binette et al. (1996).

Other parameters entering the models are the following:

a) The $A_{M/IB}$ parameter is defined as the ratio between the solid angle occupied by the MB component and the solid angle of the IB component. $A_{M/IB}$ can vary with nuclear distance (as would the covering factor in traditional models). In the case of description (1) above, $A_{M/IB}$ must be ≥ 1 since the MB clouds (with direct view of the central source) surround the IB clouds, acting as a gaseous envelope. This is not the case for description (2) above in the event that a large fraction of the inner MB component (as postulated for the hidden BLR in Seyfert 2) would have its view hidden by a dusty torus near the plane of the sky; in this case the apparent $A_{M/IB}$ could be $\ll 1$.

b) To define the thickness of the MB envelope (or cloud) we use the parameter F_{MB} , which is the fraction of ionizing photons absorbed in the MB component. For definiteness, this value was kept at $F_{MB} = 0.35$ (cf. Binette et al. 1996) for both galaxies. This depth corresponds to the peak in heating efficiency.

c) Because the [S II] emission is produced entirely within the IB component, the IB gas densities n_{IB} at any radial position were derived from the measured [S II] $\lambda 6731$ /[S II] $\lambda 6717$ line ratio ($R_{S II}$). Hence, this is generally not a free parameter.

d) The density jump parameter is $S_{I/M} = n_{IB}/n_{MB}$, where n_{MB} is the density of the MB component.¹ In Binette et al. (1996) $S_{I/M}$ was constant at 20. In this paper, its value is set by the value U_{MB} (described below) and by the value inferred for n_{IB} .

e) The ionization parameter of the MB clouds U_{MB} is the only one we need to define a priori. The ionization parameter of the IB clouds, U_{IB} , on the other hand follows from its relation with U_{MB} : $U_{IB} = (1 - F_{MB})U_{MB}S_{I/M}^{-1}$. We emphasize that, in our approach, selecting a value for U_{MB} is not as critical to the line emission ratios as in single-component models. In effect, if we define “excitation” as representing the relative importance of high-excitation lines relative to low-excitation lines, it follows that the line excitation in this scheme is directly set by $A_{M/IB}$ (the proportion of high- vs. low-excitation clouds).

f) Mostly we have used solar metallicities Z_\odot for all chemical elements. In some cases we have explored the possibility of a radial variation of the abundances.

g) For definiteness, we assumed in all models an almost negligible dust-to-gas ratio of $\mu = 0.015$ as in Binette et al. (1996; the solar neighborhood value is $\mu = 1$). Inclusion of dust causes a slight increase of the $T_{O III}$ temperature of the MB clouds but do not affect significantly the emission-line spectra.

h) The adopted geometric dilution parameter is $w_{dil} = (r_*/2r_w)^2$ (Swihart 1969), where r_* is the source radius (as a

¹ In the case of the alternative description 2, $S_{I/M}$ represents the increase in dilution of the nuclear radiation as the IB clouds lie farther out than the intervening MB clouds.

numerical convenience we adopted 1 lt-day in the calculations) and r_w is the distance between the center of the extraction window (defined in § 2) and the nuclear source. This parameter translates the intensity of ionizing photons emitted at the source surface to the *mean intensity* of ionizing photons available at different distances from the nuclei. According to the geometries proposed in § 4, we are probably observing physical distances along the direction of the cone which are close to the true values in the case of ESO 362-G18, which lies approximately along the major axis, while in ESO 362-G8, the direction of the blob apparently makes an angle $\approx 30^\circ$ with the plane of the sky. We may be thus underestimating the distances to the external blob by $\approx 15\%$.

i) The effective photon flux as a function² of r_w is simply $Q(H^0)/(4\pi r_w^2)$, where $Q(H^0)$ is the photon luminosity (quanta s^{-1}) of the ionizing source integrated over 4π (see also § 6.2). Intrinsically, the nuclear source is considered isotropic. This implies that we consider the ionizing cones due to a highly opaque dusty torus near the source which effectively collimates the photons to the opening angle observed. In our approach, the value of $Q(H^0)$ is not an independent quantity, but is derived implicitly from the adopted value of U_{MB} and n_{MB} at some reference nuclear distance (we recall that $n_{MB} = n_{IB}/S_{I/M}$, where n_{IB} is measured from $R_{S_{II}}$). This procedure for inferring $Q(H^0)$ is equivalent to that followed by Storchi-Bergmann, Mulchaey, & Wilson (1992a) in deriving

² Hence the ionization parameter is defined as $U_{MB} = Q(H^0)/(4\pi r_w^2 n_{MB} c)$, where c is the speed of light.

the UV luminosity from their Seyfert sample except that it is adapted here to the MB versus IB cloud dichotomy.

The results of the photoionization model calculations are shown together with the observed values as a function of distance from the center in Figures 10 and 11. The values of the model parameters which best reproduce the observed line ratios are listed in Tables 2 and 3.

Having outlaid how our models are constrained by the spatial run of observed line *ratios*, we have performed independent consistency checks about other derived quantities like the volume filling factor, ϵ , and the covering factor, C , as a function of radius, both of which depend in turn on line *fluxes* and must strictly remain smaller than unity at all positions. This turns out to be the case as later shown, confirming that the run of physical parameters inferred about the MB and IB components is self-consistent.

The covering factor C for each window was calculated as the ratio between the observed luminosity $L(H\beta)$ and the expected (that is, for $C = 1$) luminosity $L(H\beta)^{model} = A\mathcal{L}(H\beta)_{MB} + A\mathcal{L}(H\beta)_{IB}$, where A is the cross-sectional area of the window facing the source and $\mathcal{L}(H\beta)_{MB}$ and $\mathcal{L}(H\beta)_{IB}$ are the luminosities per unit area from the photoionization calculations. In order to evaluate A , we have adopted a conical geometry for the emitting gas such that $A = l2rtg(\theta)$, where l is the linear extent at the galaxy corresponding to $2''$ (slit width), r is the distance between the center of the window and the source, and θ is half the opening angle of the cone (we adopted $\theta = 27.5^\circ$ for ESO 362-G8 and $\theta = 40^\circ$ for ESO 362-G18 using the narrowband images of Mulchaey et al. 1996).

TABLE 2
ENLR MODEL PARAMETERS^a FOR ESO 362-G18

Position	n_{IB} (cm^{-3})	$S_{M/I}$	n_{MB} (cm^{-3})	Z_N^b (Z_\odot)	$A_{M/I}$	w_{dil}	$\log L(H\beta)^c$ ($ergs\ s^{-1}$)
NW2"	1200	20	60	1.5	9	1.613×10^{-11}	39.90
NW5"	220	4	55	0.5	1	2.581×10^{-12}	39.16
NW10"	180	4	45	0.5	1	6.453×10^{-13}	38.91
NW17"	140	4	35	0.5	1	2.233×10^{-13}	38.68
SE2"	1200	20	60	1.5	7	1.613×10^{-11}	39.90
SE5"	220	4	55	0.5	1.5	2.581×10^{-12}	39.18
SE10"	180	4	45	0.5	5	6.453×10^{-13}	38.70
SE17"	140	4	35	0.5	5	2.233×10^{-13}	37.94

^a $F_{MB} = 0.35$ at all locations.

^b Nitrogen abundance.

^c Observed $H\beta$ luminosity.

TABLE 3
ENLR MODEL PARAMETERS^a FOR ESO 362-G8

Position	n_{IB} (cm^{-3})	$S_{M/I}$	n_{MB} (cm^{-3})	Z_N^b (Z_\odot)	$A_{M/I}$	w_{dil}	$\log L(H\beta)^c$ ($ergs\ s^{-1}$)
SW2"	980	10	98	1.5	2.8	1×10^{-11}	39.80
SW4"	735	30	24.5	1.5	2	2.5×10^{-12}	38.62
SW6"	326	30	10.88	1.5	1.5	1.12×10^{-12}	37.61
NE2"	980	10	98	1.5	2.3	1×10^{-11}	40.24
NE4"	735	30	24.5	1.5	2	2.5×10^{-12}	38.90
NE6"	326	30	10.88	1.5	4	1.12×10^{-12}	37.87
NE9"	145	30	4.84	1.5	5	4.93×10^{-13}	38.88
NE14"	60	30	2	1.5	4	2.04×10^{-13}	38.49

^a $F_{MB} = 0.35$ at all locations.

^b Nitrogen abundance.

^c Observed $H\beta$ luminosity.

The filling factor ϵ is the ratio between the volume effectively occupied by the gas and the volume V of the window and can be calculated as follows (Osterbrock 1989):

$$\epsilon_{\text{MB}} = \frac{L(\text{H}\beta)_{\text{MB}}}{V \alpha_{\text{H}\beta}^{\text{eff}} h\nu_{\text{H}\beta} n_{\text{MB}}^2}, \quad (1)$$

where $L(\text{H}\beta)_{\text{MB}}$ is given by the expression below, $V = Aw$, w being the linear extent of the window (Table 1), $\alpha_{\text{H}\beta}^{\text{eff}}$ is the effective $\text{H}\beta$ recombination coefficient (the temperature dependence is taken care by MAPPINGS Ic),

$$L(\text{H}\beta)_{\text{MB}} = \frac{A_{\text{M}/\text{I}} C_{\text{M}/\text{I}} L(\text{H}\beta)}{(1 + A_{\text{M}/\text{I}} C_{\text{M}/\text{I}})}, \quad (2)$$

where $C_{\text{M}/\text{I}}$ is the ratio between the $\text{H}\beta$ luminosities of the MB and IB components from the model (Binette et al. 1997) and $L(\text{H}\beta)$ is the total observed $\text{H}\beta$ luminosity. The value of $L(\text{H}\beta)_{\text{IB}}$ is the difference between $L(\text{H}\beta)$ and $L(\text{H}\beta)_{\text{MB}}$ and was used to calculate ϵ_{IB} using the same procedure outlined above for ϵ_{MB} .

We have used the observed $\text{H}\beta$ luminosity for each extraction window to calculate the total gas mass as a function of the distance from the nucleus. The masses of the MB and IB components were calculated separately, using the expressions above for $L(\text{H}\beta)_{\text{MB}}$ and $L(\text{H}\beta)_{\text{IB}}$.

The MB clouds gas mass is given by (Osterbrock 1989)

$$M_{\text{MB}} = \epsilon_{\text{MB}} V n_{\text{MB}} m_{\text{H}}, \quad (3)$$

where m_{H} is the mass of the proton. Using the above equation (1) for ϵ_{MB} , we obtain

$$M_{\text{MB}} = \frac{L(\text{H}\beta)_{\text{MB}} m_{\text{H}}}{\alpha_{\text{H}\beta}^{\text{eff}} h\nu_{\text{H}\beta} n_{\text{MB}}}. \quad (4)$$

Similarly, for the IB clouds we obtain

$$M_{\text{IB}} = \frac{L(\text{H}\beta)_{\text{IB}} m_{\text{H}}}{\alpha_{\text{H}\beta}^{\text{eff}} h\nu_{\text{H}\beta} n_{\text{IB}}} f, \quad (5)$$

where f is a computed correction factor which allows for the existence of a partially ionized zone (in which case the total gas mass is higher than that of the ionized gas alone); f should be considered a lower limit since deeper layers of neutral (or molecular) gas may well exist beyond the Strömgen depth as a result of the UV shielding by the IB component.

6.1. Results for ESO 362-G18

One of our goals was to construct a self-consistent model based on the assumptions of the unified model. For ESO 362-G18, which is a Seyfert 1 galaxy, we should directly observe in the optical the continuum of the central source if it extends to this spectral region. This was confirmed in § 3, where we pointed out that the observed continuum could be fitted by a power law $F_{\nu} \propto \nu^{-0.76}$.

We have tried to use the optical fluxes together with the X-ray flux in order to constrain the flux of the ionizing continuum. Rush et al. (1996) give the flux in the soft X-ray obtained with *ROSAT*, using $F_{\text{X}} \propto \nu^{-1.2}$. A simple power law connecting the optical and soft X-rays has too steep a slope ($\alpha \sim -1.6$) and did not produce enough ionizing photons to reproduce the observed line ratios and fluxes. This result is not affected significantly when we allow for the possible range of temporal variations of the X-ray flux rela-

tive to the optical flux, considering that they were not obtained simultaneously.

We then tried as ionizing continuum the multisegmented power law of MFK which we normalized to our observed optical continuum. This continuum together with the observed optical spectrum and X-ray flux is illustrated in Figure 12. Although this continuum has a dip in the soft X-ray region, the *ROSAT* flux is still much smaller, suggesting that the soft X-rays are absorbed in this galaxy. The resulting source luminosity L_{ν} (illustrated by the dotted line in Fig. 12) has 2.1×10^{54} ionizing photons. The best photoionization model using the MFK continuum requires $U_{\text{MB}} = 0.018$ (which implies $n_{\text{MB}} = 60 \text{ cm}^{-3}$) within $2''$. Nevertheless, such models failed to reproduce simultaneously $R_{\text{O III}}$, $[\text{O III}]/\text{H}\beta$, and $[\text{Ne v}] \lambda 3426/\text{H}\beta$ observed in the inner $2''$ (466 pc). Models with even higher U_{MB} , up to 0.055 (see Fig. 12), were also tried but did not improve the results. We then conclude that the MFK continuum is not adequate to represent the true continuum observed by the ENLR of this galaxy.

Based on the success of previous modeling by Binette et al. (1996), we have then adopted as ionizing continuum a simple power law with the same spectral index as the X-ray observations ($\alpha = -1.2$), which is shown as a solid line in Figure 12. With $U_{\text{MB}} = 0.018$ within $2''$, we have successfully reproduced most emission-line ratios, as illustrated in Figure 10 (and also $[\text{Ne v}]/\text{H}\beta$, although not shown in this figure) using this continuum.

From Figure 12 it can be seen that the adopted power-law continuum (which has $\approx 8.5 \times 10^{53}$ ionizing photons) is ~ 3 times brighter in the optical than the observed. Nevertheless, if we extrapolate the observed optical power law to 1 ryd, its luminosity turns out smaller than that of the adopted power law by only 40% ($L_{\nu}^{\text{PL}}/L_{\nu}^{\text{opt}} = 1.4$). The two values would agree if we assume that the optical continuum is reddened by $E(B-V) = 0.14$, which is consistent with the reddening derived from the broad Balmer lines $\text{H}\alpha/\text{H}\beta$ under the assumption that the unreddened ratio is 3.1. In this case, the optical continuum could be fitted by a power law $F_{\nu} \propto \nu^{-0.54}$ (after the reddening correction), and its extrapolation to ν_0 would give the same L_{ν} as the power-

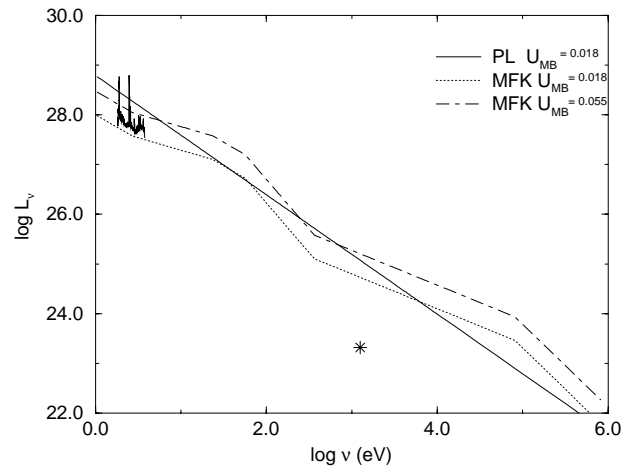


FIG. 12.—Power law and segmented power law (MFK) used as ionizing continua in the models for ESO 362-G18 (and identified in the upper corner of the figure). Also shown are the observed optical spectrum (for $0.25 < \log \nu < 0.6$, including the emission lines) after subtraction of the stellar population contribution and the observed X-ray luminosity (*star symbol*).

law continuum adopted in the modeling. Another possibility to explain the inferred flatness in the optical is the presence of a blue bump which would roll off to a steeper power law beyond 1 ryd. In any event, following a $UBVRI_c$ photometric survey, Winkler (1997) suggests that in ESO 362-G18 this bump is either weak or absent. We conclude that the observed optical and the ionizing continua of the model can be reconciled within the uncertainties.

A much larger discrepancy is observed in the X-ray domain where the soft X-rays (at 1.25 keV) appear to be $\sim 10^2$ times weaker than the power law of the model. This suggests that the ENLR might be seeing a different ionizing continuum than the one inferred by using the observed flux level in the X-rays. As mentioned above, this could be understood if there was a large column of intervening H I (intrinsic to the Seyfert) along our line of sight to its nucleus but which would be absent between the nuclear source and the ENLR region. Such a discrepancy between the ionizing continuum and the *ROSAT* flux has been found in other works. In particular, it is very similar to that found by Alexander et al. (1999) between the modeled power-law continuum and the *ROSAT* fluxes of NGC 4151 (Edelson et al. 1996) for which the *ROSAT* spectrum is clearly absorbed.

The observed and modeled line ratios with the power-law continuum are shown in Figure 10. The observed $[\text{O III}]/\text{H}\beta$ is strongly variable through the ENLR. We have thus assumed that U_{MB} varies with distance from the nucleus as shown in Figure 13, together with U_{IB} . The resulting n_{MB} shows a smooth decrease with distance from the nucleus (from 60 cm^{-3} at $2''$ to 35 cm^{-3} at $17''$; see Fig. 13). The decrease of the geometric dilution parameter dominates the derived decrease in U_{MB} .

From Figure 13, it can be observed that $S_{\text{I/M}}$ is large within $2''$ (20) and smaller farther out ($S_{\text{I/M}} = 4$). The behavior of $A_{\text{M/I}}$ (larger in the nuclear and cone regions) is consistent with the higher excitation gas around the nucleus and cone, indicating a larger contribution of the low-density gas of the MB component at these locations. Figure 14 indeed

shows a smaller mass of IB component relative to the MB component in the nuclear region and also in the cone direction when compared to the opposite side. No difference in temperatures was derived for the two sides, although the excitation (see, e.g., $[\text{O III}]/\text{H}\beta$) is very different. This result shows that no other source of ionization (e.g., shocks) is needed to explain different degrees of excitation of the gas when we allow for the variation of the relative contribution of the MB and IB clouds through the $A_{\text{M/I}}$ parameter.

The modeled ratios which show the largest differences when compared to the observations are $[\text{N II}]/\text{H}\alpha$, $[\text{N II}]/[\text{O II}]$, and $[\text{S II}]/\text{H}\alpha$ (to the northwest). In order to improve the modeling, we have changed the element abundances considering the results of Storch-Bergmann et al. (1996a, 1996b) where it was concluded that Seyfert host galaxies present similar radial abundance gradients to that observed for normal galaxies. For a typical gradient of $0.075 \text{ dex kpc}^{-1}$, a nuclear solar abundance implies an abundance of $0.5 Z_{\odot}$ at 4 kpc. Nitrogen was concluded to behave as a secondary element with its abundance given by a relation presented in Storch-Bergmann, Calzetti, & Kinney (1994). Using that relation, we obtain that, for a solar abundance of oxygen, the nitrogen abundance is 1.5 times solar, while for oxygen abundance 0.5 times solar the nitrogen abundance is also approximately 0.5 times solar. In order to investigate the effects of a varying abundance we have considered two possibilities: for $r \leq 2''$, we have adopted the abundances of all elements as solar, except the nitrogen abundance, which was adopted as 1.5 solar. For larger radii, we have adopted abundances of 0.5 times solar for all elements. We show the results of this new model in Figure 10 using dashed lines. Only the ratios for which there is significant improvement over our previous model are presented. A better fit to the line ratios involving the nitrogen lines at $r \geq 5''$ was obtained with a selective underabundance of nitrogen of 0.5 the solar value, keeping the abundance of the other elements at the solar value. Improvement is seen for $[\text{N II}]/\text{H}\alpha$, $[\text{N II}]/[\text{O II}]$, and

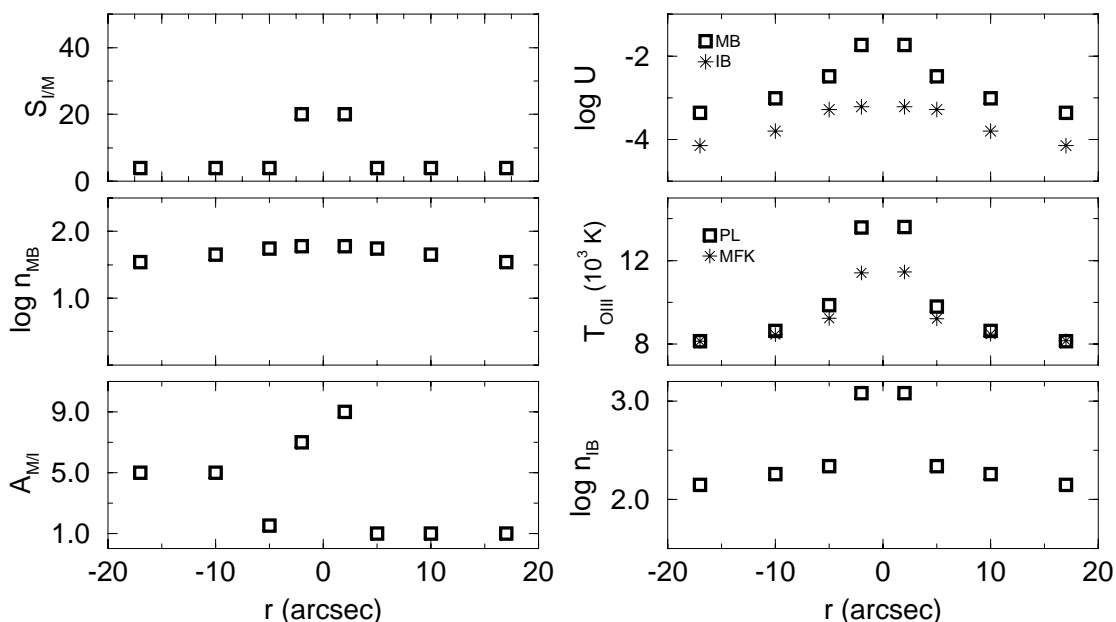


FIG. 13.—Modeled parameters as a function of distance from the nucleus (along P.A. 158°) for ESO 362-G18. Negative r is to the southeast (cone), and positive r is to the northwest.

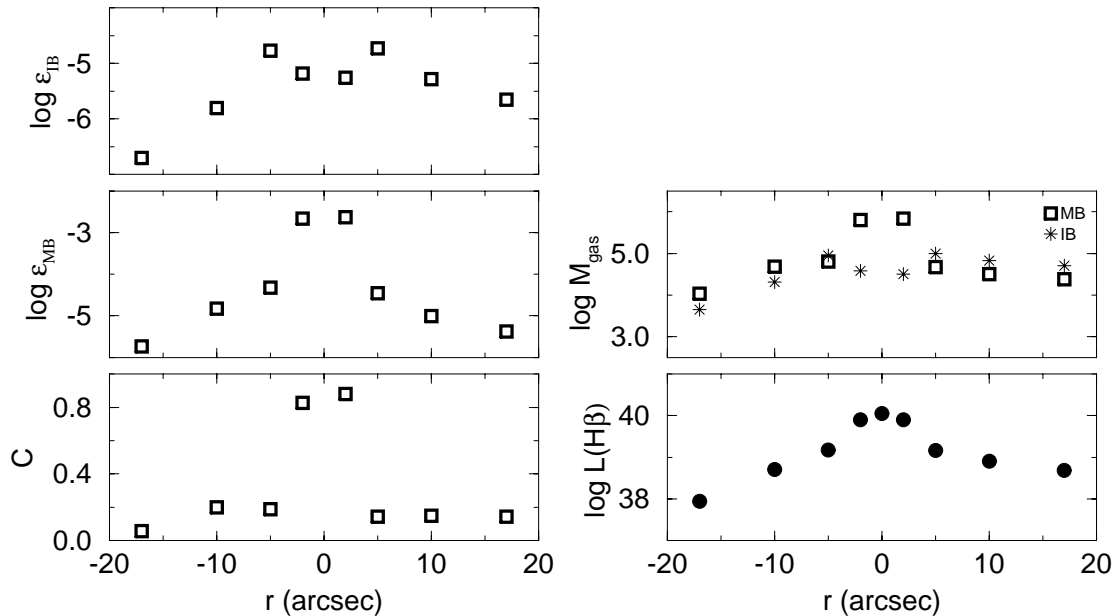


FIG. 14.—Parameters derived from the models for ESO 362-G18: filling factors ϵ_{IB} and ϵ_{MB} , covering factor C , mass M (of MB and IB clouds), and luminosity $L(\text{H}\beta)$ (in 10^{40} ergs s^{-1}) as a function of distance from the nucleus (P.A. 158°). Negative r is to the southeast (cone), and positive r is to the northwest.

$[\text{N II}]/[\text{O III}]$, but we do not know why nitrogen should be selectively underabundant outside the nucleus.

We point out that one of our goals in modeling the ENLR was to test the MB/IB model with a larger number of constraints than in previous works. This was accomplished by simultaneously fitting all the ENLR extraction windows and by assuming on both sides of the nucleus the same properties for the ionizing continuum and for the ENLR (to the extent that the observations appear to support this possibility). For instance, the densities of either the MB or the IB component are the same at symmetric positions around the nucleus as well as the metallicities (and the unconstrained dust-to-gas ratio). This in turn implies that the density jump parameter $S_{\text{I/M}}$, the temperature $T_{\text{O III}}$, and the thickness of the MB component have all the same radial dependence on both sides of the nucleus. The only parameter that was left free to vary with position was $A_{\text{M/I}}$, although its value at $2''$ from the nucleus could be anchored by requiring that the model matches the $\text{He II}/\text{H}\beta$ which could be observed only in that location.

In Figure 14, we show the behavior of the filling factors ϵ_{MB} and ϵ_{IB} as a function of distance from the nucleus. The ϵ_{IB} has a minimum at the inner regions, peaks at $5''$ at both sides of the nucleus, and decreases farther out. The ϵ_{MB} peaks near the nucleus and decreases outward. The ϵ_{MB} is typically 1.5 orders of magnitude larger than ϵ_{IB} . The same figure also shows the covering factor C of the gas contained in each extraction window. Its value reaches ≈ 0.8 at $2''$ and shows a sharp decrease outward ($C \sim 0.2$).

Finally, the mass distribution of the MB clouds (Fig. 14) peaks near the nucleus and dominates the total mass within $2''$ from the nucleus, decreasing outward, while the IB clouds presents a minimum at the inner regions, a small peak at $5''$, and decreases beyond this radius, with lower values at the cone as compared to the opposite side. The mass of the MB clouds is larger than that of the IB clouds at the cone region, the opposite happening at the other side.

6.2. Results for ESO 362-G8

In order to infer the luminosity of the source in this Seyfert 2 galaxy we have assumed that the path between the source and the external blob is free from absorption and that the source is isotropic. The $\text{H}\beta$ luminosity of the blob was then used to calculate the approximate number of ionizing photons $Q(\text{H}^0)$ (Osterbrock 1989):

$$Q(\text{H}^0) \approx \frac{\alpha_B(\text{H}^0, T)}{\alpha_{\text{H}\beta}^{\text{eff}}(\text{H}^0, T)} \frac{L(\text{H}\beta)}{h\nu_{\text{H}\beta}} \frac{4\pi}{\omega}, \quad (6)$$

where ω is the solid angle covered by the blob. The adopted value is $\omega = 0.21\pi$ from inspection of the narrowband images of Mulchaey et al. (1996). The quantity $Q(\text{H}^0)$ was used in a initial attempt to normalize the luminosity of the ionizing continuum. A posteriori, it was concluded that in order to reach the necessary ionization parameter of the MB cloud component U_{MB} , we needed a luminosity ≈ 10 times larger, or in other words, the covering factor *inside* the blob is inferred to be approximately 10%–20%.

The two ionizing continuum distributions MFK and power law $F_\nu = k\nu^{-1.2}$ reproduced the overall behavior of the observed emission-line ratios except for $[\text{O III}] \lambda 4363/[\text{O III}] \lambda 5007$ (hereafter $R_{\text{O III}}$) and to some extent $[\text{O III}]/\text{H}\beta$. We illustrate this in Figure 11 by showing the lower $[\text{O III}]/\text{H}\beta$ ratios obtained with the MFK continuum and in Figure 15 by showing the derived temperatures $T_{\text{O III}}$ for the power law and MFK continua. It can be observed that the temperatures attained with the MFK continuum are significantly smaller than those with the power law. Only with the latter continuum is it possible to reach the high $T_{\text{O III}}$ observed ($R_{\text{O III}} = 0.02$) at NE9''. In effect, the power-law model predicts a $R_{\text{O III}}$ which is only 20% smaller while at the same time fits well the high $[\text{O III}] \lambda 5007/\text{H}\beta$ of the blob. On the other hand, with the MFK continuum, even when using a much larger U_{MB} (e.g., 0.05–0.06 as in Binette et al. 1996), we were not able to reproduce the data.

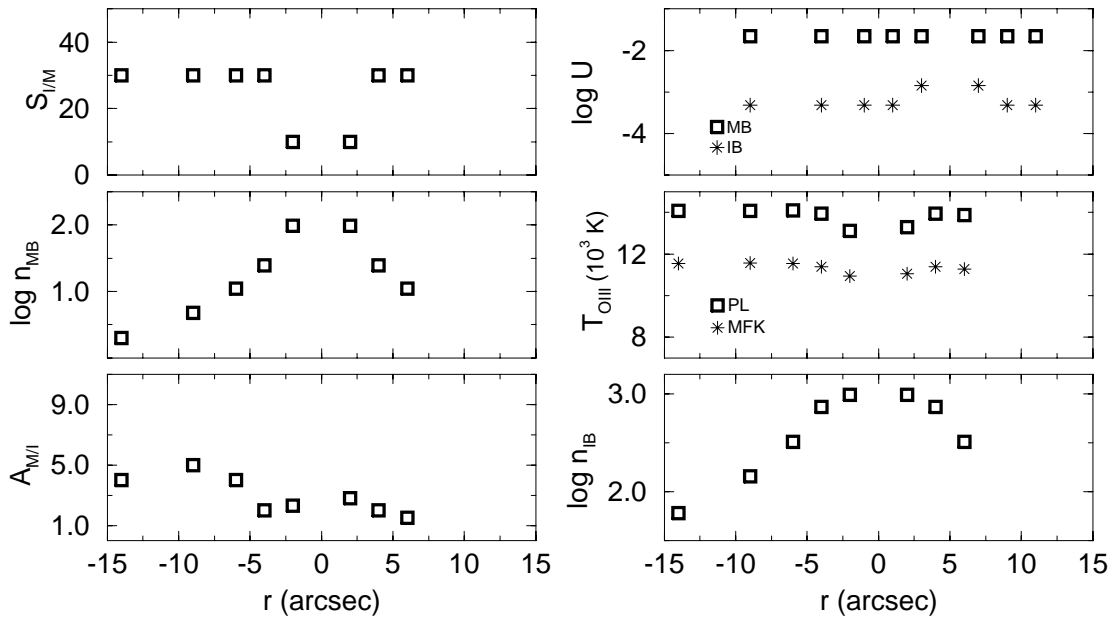


FIG. 15.—Modeled parameters as a function of distance from the nucleus (P.A. 60°) for ESO 362-G8. Negative r is to the northeast (blob), and positive r is to the southwest.

Using the power-law continuum above as the ionizing spectrum, in order to simultaneously reproduce the observed $[\text{O III}](\lambda\lambda 5007+4959)/\text{H}\beta$ as well as $R_{\text{O III}}$ and to maintain $C < 1$ at all locations (see below), it was necessary to adopt $U_{\text{MB}} = 0.022$, implying a number of ionizing photons for the nuclear source of $2.7 \times 10^{54} \text{ s}^{-1}$. We can now use this photon luminosity to extrapolate the power-law continuum to the optical in order to estimate the obscuration to the nuclear source. This gives a flux of $1.73 \times 10^{-14} \text{ ergs s}^{-1} \text{ cm}^{-2}$ at 3500 \AA . A comparison of this flux with 5% of the observed optical continuum (which is the upper limit attributed to the contribution of the nuclear continuum in § 3) gives a minimum obscuration to the central source of $A_V \approx 4.0$ mag.

It can be observed in Figure 11 that $[\text{O III}]/\text{H}\beta$ is approximately constant throughout the ENLR. We have thus assumed that U_{MB} does not vary with distance. This was accomplished in the models by imposing that the density of the MB component varied as $n_{\text{MB}} \propto r^{-2}$, where r is the distance to the nucleus. Given that n_{IB} is set by the $[\text{S II}] \lambda 6731/[\text{S II}] \lambda 6717$ ratio, the parameter $S_{M/I}$ ($=n_{\text{IB}}/n_{\text{MB}}$) by definition varied accordingly with position.

In order to reproduce the behavior of the line ratios, we have varied the parameter $A_{M/I}$ (while keeping constant U_{MB} and deducing n_{IB} from the observed $[\text{S II}]$ doublet; see Fig. 15). Values of $A_{M/I} \approx 4$ are favored at the blob while values of $A_{M/I} \approx 2$ are indicated elsewhere, implying that the blob has a larger relative contribution of MB clouds, as expected due its larger excitation. We note that $U_{\text{IB}} = 0.0005$ at the two inner points near the nucleus, while it is 3 times larger outside ($U_{\text{IB}} = 0.0014$; these values are constrained via the $[\text{S II}] \lambda 6731/[\text{S II}] \lambda 6717$ ratio). The behavior of both n_{MB} and n_{IB} with distance is shown in Figure 15.

In Figure 16, we show the behavior of the filling factors ϵ_{MB} and ϵ_{IB} as a function of distance from the nucleus. Although both filling factors decrease radially away from the nucleus, there is a sharp increase at the position of the external blob. The behavior of the filling factors mimic to a

large extent that of $L(\text{H}\beta)$, as can be expected. Interestingly, the value of $\epsilon_{\text{MB}} \approx 10^{-2.7}$ is much larger at the blob than anywhere else as a result of the apparent dominance of the MB component at that location. The fact that we can fit the ratios and the brightness of this conspicuous distant blob by varying only $A_{M/I}$ and ϵ by relatively small amounts (relative to nuclear values) is consistent with the existence of a powerful but hidden nuclear source, in accordance with the unified model. Figure 16 also shows the covering factor C of the gas contained in each extraction window. Its value reaches ≈ 0.6 at NE2'' and presents a secondary maximum with $C \approx 0.1-0.16$ at the blob.

Finally, the mass distribution of both the MB and IB clouds (Fig. 16) peaks near the nucleus and at the blob location as well (but less prominently in the case of the IB component). Interestingly, the MB component inside the blob dominates in mass over all other locations, including the nucleus.

We can compare the filling factors obtained here with those from previous works. In the case of radio galaxies, the values encountered by van Breugel et al. (1985) and Heckman et al. (1982) using the $\text{H}\alpha$ or $\text{H}\beta$ luminosity, emission region size, and gas density inferred from the $[\text{S II}]$ doublet were centered around $\sim 10^{-5}$ with a significant dispersion. As can be seen in Figures 14 and 16, the filling factor of the IB component in our model lies in the range $10^{-6.6}-10^{-4.7}$. (Within a factor of 2, this IB value is the same as that of single-component models.) However, if we allow for the existence of a high-excitation MB component of low density, we derive significantly larger filling factors, especially in the nucleus where the values reach $\epsilon_{\text{MB}} > 10^{-3}$. Even such large values are beyond the spatial resolution of the best telescopes; therefore, the smoothness of narrow-band images taken so far in no way can weaken our proposition that the fine structure of the emission gas consists of very small MB clouds (and of IB cores).

One could ask how these two phases can come about and coexist (albeit inside very large and possibly disconnected

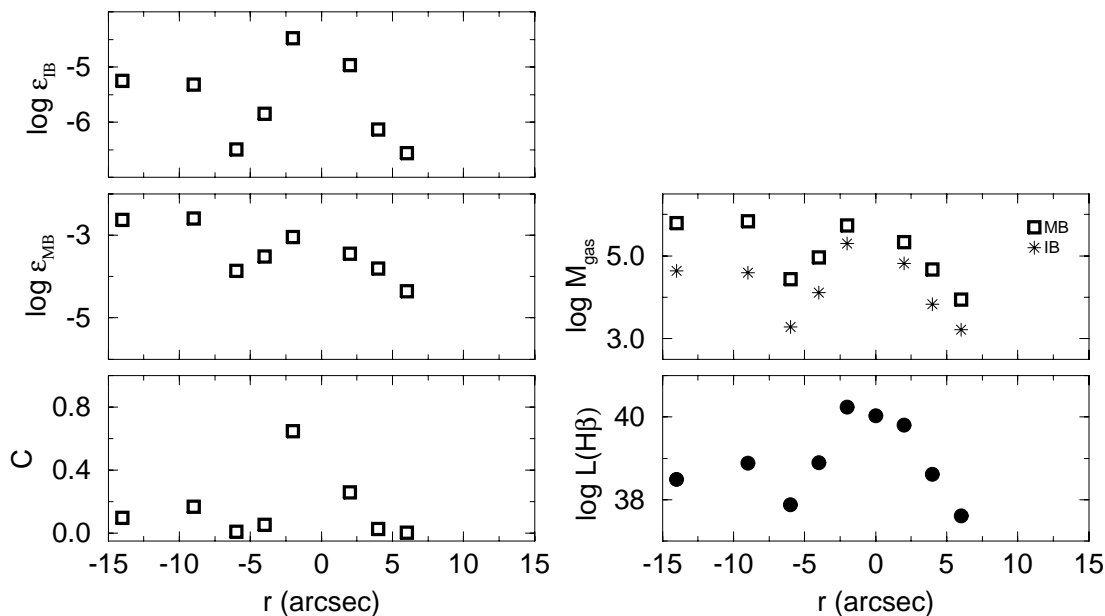


FIG. 16.—Parameters derived from the models for ESO 362-G8: filling factors ϵ_{IB} and ϵ_{MB} , covering factor C , mass M (of MB and IB clouds), and luminosity $L(\text{H}\beta)$ (in 10^{40} ergs s^{-1}) as a function of distance from the nucleus (P.A. 60°). Negative r is to the northeast (blob), and positive r is to the southwest.

volumes) without being in pressure equilibrium. We propose the following nonstatic scenarios. In the case of description 1, if we assume that the strong nuclear ionizing radiation is eating away at the clouds, this erosion would lead to the existence of an internal ionizing front which, depending on the rate of excess photons supplied by the erosion, would be propagating significantly faster into the cloud than that of the density wave (or D-type front) which equalizes the gas pressure but lags behind (at a speed confined to the sound speed). The IB/MB boundary would correspond to the position of this density (jump) front. With description 2, the dynamical pressure generated by shocks could be important and in some regions exceed that of the thermal hot phase which otherwise confines the clouds, thereby generating regions of different pressures (dynamically confined).

7. SUMMARY AND CONCLUDING REMARKS

In this paper we have investigated the continuum and emission-line properties of the ENLR of the Seyfert 1 galaxy ESO 362-G18 and Seyfert 2 galaxy ESO 362-G8 using optical long-slit spectra.

The stellar and gas kinematics, combined with the images of Mulchaey et al. (1996), suggest the following scenarios for the orientation of the nuclear engines relative to the galaxies within the framework of the unified model. For the Seyfert 1 galaxy ESO 362-G18, the nuclear collimation axis makes an angle with the disk smaller than half the opening angle of the cone of radiation escaping from the nucleus so that it ionizes gas in the disk along P.A. 158° , giving origin to the cone-shaped region observed in the $[\text{O III}]$ image.

For the Seyfert 2 galaxy ESO 362-G8, the nuclear collimation axis is almost perpendicular to the disk and the collimated nuclear radiation ionizes a high-latitude cloud (the high-excitation blob in the $[\text{O III}]$ image) which is being blown away from the galaxy disk. Since the derived mass for the blob (see below) and the measured velocities are

consistent with those observed in starbursts (Heckman, Armus, & Miley 1990), we speculate that this blob has its origin in superwinds associated with a poststarburst observed within 1.5 kpc from the nucleus. Using the observed velocity and distance between the blob and the nucleus, simple estimates are consistent with the gas in the blob being expelled from the burst when it was active, ~ 300 Myr ago.

We have used the stellar population spectra obtained from external regions, which are approximately free from emission lines, to subtract the contribution of the stellar component from the nuclear spectra and thereby isolate the nuclear continuum. For the Seyfert 1 galaxy ESO 362-G18, the derived continuum is a featureless power law $F_\nu \propto \nu^{-0.76}$. For the Seyfert 2 galaxy ESO 362-G8, we did not find evidence for a nuclear featureless continuum contributing more than 5% in the near-UV. Instead, we found that the dilution observed in the nuclear values of equivalent widths of the stellar absorption features is due to a ~ 300 Myr stellar population within $5''$ from the nucleus. This result shows that a blue continuum is not necessarily due to only an AGN featureless spectral distribution or to a very young burst of star formation and supports the findings of Schmitt et al. (1997) (who used spectral synthesis) that an intermediate-age stellar component is frequently found in the nuclear region of Seyfert 2 galaxies.

Emission-line fluxes were measured up to $17''$ (≈ 4 kpc from the nucleus) for ESO 362-G18 along the cone direction (P.A. 158°), for which the excitation is high within $2''$ from the nucleus and in the cone region (southeast) but decreasing more rapidly in the other directions. In ESO 362-G8, for which the excitation is high around the nucleus and in the blob, emission-line fluxes have been measured up to $14''$ (4.2 kpc) toward the blob direction and $6''$ (1.8 kpc) to the opposite side.

We have modeled the extended emission as a radial sequence of clouds comprising a mixture of MB and IB

components. We have used the photoionization code MAP-PINGS Ic, in which the diluted nuclear radiation ionizes the MB component, is filtered by it, and then ionizes the IB component (Binette et al. 1996).

Two possible ionizing spectra have been considered: the broken power law of Matthews & Ferland (1987), revised by Korista et al. (1997), and a single power law $F_\nu \propto \nu^{-1.2}$. Only with the power law was it possible to reproduce the high-excitation line fluxes observed in the spectra closest to the nucleus. For the Seyfert 1 galaxy ESO 362-G18, the inferred luminosity of the power-law ionizing continuum can be reconciled with the observed one in the optical if we allow for a different slope in the UV respective to the optical and for the presence of a small reddening obscuring the nuclear source and BLR. However, it is not possible to reconcile the power-law luminosity with the observed soft X-ray flux which is about 100 times less luminous than the ionizing continuum. This suggests that the latter is absorbed in the direction of the Earth, similarly to what seems to be happening in NGC 4151 (Alexander et al. 1999).

For the Seyfert 2 galaxy ESO 362-G8, despite not seeing the nuclear source, we inferred a number of ionizing photons of 2.7×10^{54} , approximately 3 times larger than that of ESO 362-G18. An estimate of the nuclear obscuration in ESO 362-G8 gives $A_V \geq 4.0$ mag.

From the models, the high-excitation cone in ESO 362-G18 can be understood as a structure with a larger relative mass contribution from the lower density MB clouds as compared with the other side of the galaxy. The model allows us to obtain different distributions of emitting mass on each side of the nucleus even though the bulk density distribution (constrained by the [S II] ratio) is the same. Such discrimination is possible only with multi-component models. In fact, in our models we adopt a central ionizing source with isotropic properties (e.g., only one dilution law) and with symmetrical physical conditions on both sides of the nucleus: densities (actually constrained by the [S II] ratio), metallicity, ionization parameter, and constant thickness of the MB component ($F_{MB} = 0.35$). The only free parameter, which was allowed to vary independently to each side of the nucleus in ESO 362-G18, was $A_{M/I}$. In the few positions where the He II $\lambda 4686/H\beta$ ratio could be measured the parameter $A_{M/I}$ was in fact set by this observed ratio.

As was found for the Seyfert 1 galaxy, the high-excitation blob in the Seyfert 2 galaxy ESO 362-G8 can be understood as due to a larger relative mass contribution from the lower density MB component as compared with the gas in the disk of the galaxy. Both near the nucleus and at the blob, the gas excitation did not vary much, which we have modeled assuming for the MB clouds a constant ionization parameter throughout the ENLR (this is equivalent to having a density variation $\propto r^{-2}$). The only free parameter was again $A_{M/I}$ whose value was determined from the He II $\lambda 4686/H\beta$ ratio measured only at 2".

We conclude by pointing out that the two-component models, besides solving the problems of large observed range of He II/H β , high $R_{O III}$, and other high-excitation line ratios (Binette et al. 1996), can produce different excitations with the same [O III] temperature, without the need of addi-

tional excitation mechanisms such as shocks. The relevant parameter is $A_{M/I}$, which in our case translates into the relative proportion of mass in MB and IB components.

What kind of observations would be crucial to test the two-component ($A_{M/I}$) model? The most direct constraint would be to resolve the emitting components of the ENLR, and measure different line ratios for the MB and IB components. On the other hand, our values for the filling factors suggest that the dimensions of these components are beyond the resolution of even the largest telescopes. But we could, in principle, measure different temperatures for the MB and IB components, as pointed out by Wilson et al. (1997). Deep observations with large telescopes should allow the measurement of the relevant emission lines (e.g., [O III] $\lambda 4363$ for the high-excitation gas and [N II] $\lambda 5755$ for the low-excitation gas). These temperature diagnostics would provide stronger constraints on the two-component model and maybe point to the need for additional components or to extra heating mechanisms like shocks. In the cases in which high temperatures are measured at locations of the ENLR coincident with strong radio emission, one could argue that the high temperatures are produced by shocks. Allen et al. (1999), for example, present line ratios for the ENLR of NGC 2992 which they reproduce by shock models. Another test for the $A_{M/I}$ model would be to measure the He II/H β ratio throughout the ENLR because the $A_{M/I}$ parameter is directly constrained by this emission-line ratio. For this to be possible, deeper exposures would again be necessary. With the available data, we could only measure this ratio at 2" from the nucleus of ESO 362-G18 and at the blob of ESO 362-G8.

Finally, we can compare the results obtained for the Seyfert 1 and Seyfert 2 galaxies. The data are consistent with similar ionizing continua, although 3 times more luminous for the Seyfert 2 galaxy. The gas around the nucleus of the Seyfert 1 galaxy presents a higher excitation than in the Seyfert 2 galaxy due a larger relative contribution of the MB component, but the gas in the cone of the Seyfert 1 galaxy presents a lower excitation than in the blob of the Seyfert 2 galaxy. Since the values of $A_{M/I}$ are comparable, this can be understood as a residual effect of using lower values of U_{MB} in our fit of the cone of the Seyfert 1 galaxy than in the blob due to a combination of lower ionizing flux and larger gas density in the disk. The total mass of ionized gas in the blob is $10^{5.8} M_\odot$, consistent with its proposed origin in a nuclear superwind being 1 order of magnitude larger than that of the cone in the Seyfert 1 galaxy disk.

This research received partial support from the Brazilian institutions CNPq and CAPES. The work of L. Binette was supported by the CONACyT grant 27546-E. We thank especially John Mulchaey for kindly making available the images for Figure 1, A. Rodríguez-Ardila for fruitful discussions, and the referee for valuable suggestions. This research has made use of the NASA/IPAC Extragalactic Database (NED), which is operated by the Jet Propulsion Laboratory, California Institute of Technology, under contract with the National Aeronautics and Space Administration.

REFERENCES

- Alexander, T., Sturm, E., Lutz, D., Sternberg, A., Netzer, H., & Genzel, R. 1999, *ApJ*, 512, 204
- Allen, M. G., Dopita, M. A., Tsvetanov, Z. I., Sutherland, R. S. 1999, *ApJ*, 511, 686
- Antonucci, R. R. J. 1993, *ARA&A*, 31, 473
- Bica, E. 1988, *A&A*, 195, 76
- Bica, E., & Alloin, D. 1986a, *A&AS*, 66, 171
- . 1986b, *A&A*, 166, 83
- Binette, L., Wilson, A. S., Raga, A., & Storchi-Bergmann, T. 1997, *A&A*, 327, 909
- Binette, L., Wilson, A. S., & Storchi-Bergmann, T. 1996, *A&A*, 312, 365
- Braatz, J. A., Wilson, A. S., & Henkel, C. 1997, *ApJS*, 110, 321
- Cid Fernandes, R., Storchi-Bergmann, T., & Schmitt, H. R. 1998, *MNRAS*, 297, 579
- Edelson, R. A., et al. 1996, *ApJ*, 470, 364
- Ferland, G. J., & Netzer, H. 1983, *ApJ*, 264, 105
- Filippenko, A. V. 1982, *PASP*, 94, 715
- González Delgado, R. M., Leither, C., & Heckman, T. M. 1999, *ApJS*, 125, 479
- Heckman, T. M., Armus, L., & Miley, G. K. 1990, *ApJS*, 74, 833
- Heckman, T. M., van Breugel, W. J. M., Balick, B., & Butcher, H. R. 1982, *ApJ*, 262, 529
- Korista, K., Ferland, G., & Baldwin, J. A. 1997, *ApJ*, 487, 555
- Matthews, W. G., & Ferland, G. J. 1987, *ApJ*, 323, 456
- Mulchaey, J. S., Wilson, A. S., & Tsvetanov, Z. 1996, *ApJS*, 102, 309
- Nazarova, L. S., O'Brien, P. T., & Ward, M. J. 1997, *A&A*, 321, 397
- Nazarova, L. S., O'Brien, P. T., Ward, M. J., & Gondhalekar, P. M. 1998, *A&A*, 331, 34
- Osterbrock, D. E. 1989, *Astrophysics of Gaseous Nebulae and Active Galactic Nuclei* (Mill Valley: Univ. Science)
- Robinson, A., et al. 1994, *A&A*, 291, 351
- Rodríguez-Ardila, A., Pastoriza, M., & Maza, J. 1998, *ApJ*, 494, 202
- Rush, B., Malkan, M. A., Fink, H. H., & Voges, W. 1996, *ApJ*, 471, 190
- Schmitt, H. R., Kinney, A. L., Calzetti, D., & Storchi-Bergmann, T. 1997, *AJ*, 114, 592
- Soares, D. S., et al. 1995, *A&AS*, 110, 371
- Storchi-Bergmann, T., Calzetti, D., & Kinney, A. L. 1994, *ApJ*, 429, 572
- Storchi-Bergmann, T., Mulchaey, J. S., & Wilson, A. S. 1992a, *ApJ*, 395, L73
- Storchi-Bergmann, T., Schmitt, H. R., Calzetti, D., & Kinney, A. L. 1998, *AJ*, 115, 909
- Storchi-Bergmann, T., Wilson, A. S., & Baldwin, J. A. 1992b, *ApJ*, 396, 45
- . 1996a, *ApJ*, 460, 252
- Storchi-Bergmann, T., Wilson, A. S., Mulchaey, J. S., & Binette, L. 1996b, *A&A*, 312, 357
- Swihart, T. L. 1969, *Astrophysics and Stellar Astronomy* (New York: Wiley)
- Unger, S. W., Pedlar, A., Axon, D. J., Whittle, M., Meurs, E. J. A., & Ward, M. J. 1987, *MNRAS*, 228, 671
- van Breugel, W. J. M., Miley, G. K., Heckman, T. M., Butcher, H. R., & Bridle, A. 1985, *ApJ*, 290, 496
- Viegas, S. M., & de Gouveia Dal Pino, E. M. 1992, *ApJ*, 384, 467
- Wilson, A. S., Binette, L., & Storchi-Bergmann, T. 1997, *ApJ*, 482, L131
- Winkler, A. S. 1997, *MNRAS*, 292, 273